CMS Physics Analysis Summary

Contact: cms-pag-conveners-smp@cern.ch 2015/07/20

Production of pairs of isolated photons in association with jets in pp collisions at $\sqrt{s} = 7$ TeV

The CMS Collaboration

Abstract

The differential cross sections for the production of a photon pair in association with jets are measured using a sample of pp collisions collected by the CMS experiment in 2011 at $\sqrt{s} = 7$ TeV, and corresponding to an integrated luminosity of 5.0 fb^{-1}. A template fit to the photon isolation distribution is used to statistically evaluate the fraction of prompt diphoton events in data. Several differential observables are studied with inclusive 1-jet and 2-jet selections. Results are compared to QCD theoretical predictions at leading and next-to-leading order.

1 Introduction

The measurement of the cross section for photon pair production in association with jets offers an important test of both perturbative and non-perturbative quantum chromodynamics (QCD). At leading order (LO), diphotons are produced via quark-antiquark annihilation $q\bar{q} \to \gamma\gamma$. At next-to-leading order (NLO), diphoton production also includes the quark-gluon channel, while next-to-next-to-leading order (NNLO) adds the gluon-gluon channel, which includes a box diagram and represents a non-negligible fraction of the total cross section[1]. Diphoton production is sensitive to the emission of soft gluons in the initial state and to the non-perturbative fragmentation of quarks and gluons to photons in the final state.

Diphoton production in association with jets represents the major source of background to the study of the Higgs boson [2–4] in the diphoton decay channel, when produced via vector boson fusion (VBF). Moreover, new physics processes may appear as deviations from the predicted diphoton spectrum in events with jets in the final state, as in gauge-mediated SUSY breaking [5]. Validating the event generators used to model the background in these analyses is therefore of crucial importance.

Differential cross sections for inclusive diphoton production have been measured by the ATLAS and CMS Collaborations using LHC data [6, 7], as well as by the CDF and D0 Collaborations using Tevatron data [8, 9]. They were found to agree with QCD predictions, with the exception of specific regions of the phase space where higher-order corrections are most relevant.

This note presents an extension of the inclusive CMS analysis [7]. The cross section is measured as a function of several photon and jet observables, separately in events with at least one or two jets in the final state. Both transverse momentum spectra and angular distributions are studied to probe the dynamics of diphoton production.

The analysis strategy pursued here closely follows that of the inclusive measurement. The main experimental challenge for the measurement of the diphoton cross section is distinguishing the "prompt" photon signal (produced directly, or as a result of fragmentation) from the background that arises from energetic neutral mesons (predominantly, π^0 and η mesons) inside jets. These mesons typically decay to two collimated photons that are reconstructed as a single photon candidate, which is referred to as "non-prompt" in this paper. The main features used to discriminate a prompt photon from a non-prompt one are the shape of the shower measured by the electromagnetic calorimeter (ECAL) [10] and the isolation energy in a cone around the photon direction [11, 12]. This information can be used to trigger on diphoton candidate events and, at the analysis level, to statistically evaluate the fraction of prompt diphoton candidates.

The CMS particle-flow (PF) reconstruction [13–15] measures individual particles produced in the collision with an optimal combination of all sub-detector information. In this process, the identification of the particle type (photon, electron, muon, charged hadron, neutral hadron) plays an important role in the determination of the particle direction and energy. The PF isolation of the selected photon candidate is used as the discriminating variable against the background. The distributions of signal and background components are built from data and used in a maximum likelihood fit to estimate the signal fraction.

After a brief presentation of the data and simulated samples used in the analysis in Section 2, the object reconstruction and selection are described in Section 3. The measurement of the diphoton signal is then described in Section 4. Corrections for resolution and efficiency are described in Section 5. Systematic uncertainties are assessed in Section 6, and the differential cross sections are presented and compared to theoretical predictions in Section 7.

2 Data and simulated samples

The data sample consists of proton-proton (pp) collision events collected at the LHC with the CMS detector in the year 2011, at a centre-of-mass energy of 7 TeV and corresponding to an integrated luminosity of 5.0 fb^{-1}.

Events are triggered [16] by requiring the presence of two photons with asymmetric transverse energy thresholds. The E_{T} trigger thresholds on the leading (sub-leading) photon are 26 (18) or 36 (22) GeV, depending on the running period. Each photon candidate is required to satisfy either loose calorimetric identification requirements, based on the shape of the electromagnetic shower, or loose isolation conditions. The trigger efficiency is evaluated using a tag-and-probe technique on $\text{Z} \to \text{e}^+\text{e}^-$ events [17], with electrons treated as photons. The trigger efficiency is measured in events that satisfy the photon preselection requirements, described in Section 3. It is measured to be between 98.8% and 100% depending on the pseudorapidity and the amount of material in front of the electromagnetic calorimeter (ECAL). The total trigger efficiency is found to be constant over the data taking period.

Several samples of simulated events are used in the analysis to validate the modeling of signal and background processes. The $\gamma\gamma$+jets signal events are generated with SHERPA 1.4.2 [18] using the CT10 [19] parton distribution functions (PDFs) set. The diagrams used in the diphoton matrix element calculation include up to three additional legs in final state. An alternative simulation of the diphoton signal is performed by generating $\gamma\gamma$+jets events with MADGRAPH 5.1 [20] (up to two jets are included at matrix element) and $\text{gg} \to \gamma\gamma$ box process events with PYTHIA. The γ+jet and QCD dijet background processes are generated with PYTHIA 6.4.24 [21], using an electromagnetic enrichment filter to obtain sufficient statistics. Drell-Yan+jets events are generated with MADGRAPH. For MADGRAPH and PYTHIA the CTEQ6L1 [22] PDFs are used. Events are processed with PYTHIA (Z2 tune) [23] for hadronization, showering of partons and the underlying event.

A detailed simulation of the CMS detector based on GEANT 4 [24] is performed for all samples, and the simulated events are finally reconstructed using the same algorithms used for data. The simulation includes the effects of in-time pileup (overlapping pp interactions within a bunch crossing) and out-of-time pileup (overlapping pp interactions from interactions happening in earlier or later bunch crossings) with a distribution matching that observed in data.

3 Reconstruction and selection

3.1 Photon reconstruction

Photon candidates are reconstructed from energy deposits in the ECAL by grouping its channels into clusters [25]. About half of the photons convert into an e^+e^- pair in the material in front of the ECAL. Electron-positron pairs are reconstructed from a combination of Gaussian-sum filter (GSF) electron tracks [26] and ECAL-seeded tracks fit to a common vertex and then matched to the photon candidate. The algorithms recover most of the energy of such converted photons. In the barrel region, superclusters are formed from five-crystal-wide strips in pseudorapidity ($\eta = -\ln[\tan(\theta/2)]$, with θ being the polar angle of the trajectory of the particle with respect to the counterclockwise beam direction), centred on the locally most energetic crystal (seed), and have a variable extension in the azimuthal direction (ϕ). In the endcaps, where the crystals are arranged according to an x-y rather than an η-ϕ geometry, groups of 5×5 crystals (which may partially overlap) around the most energetic crystals are merged if they lie within a narrow $\Delta\eta$ region. Photon candidates are reconstructed within the ECAL fiducial re-

gion $|\eta| < 2.5$, excluding the barrel-endcap transition regions $1.44 < |\eta| < 1.57$. The exclusion of the barrel-endcap transition regions ensures containment of the shower of selected photon candidates in either the ECAL barrel or one of the two ECAL endcaps. The fiducial region requirement is applied to the supercluster position (defined as the log-weighted barycentre of the supercluster's active channels) in the ECAL.

The photon energy is computed starting from the uncorrected crystal energies measured in the ECAL. The energy recorded in the preshower detector is added in the region covered by that sub-detector. The variation of the crystal transparency during the run is continuously monitored and corrected using a factor based on the change in response to light from a laser and light-emitting-diode based monitoring system. The single-channel response of the ECAL is equalised by exploiting the ϕ symmetry of the energy flow, the mass constraint on the energy of the two photons in decays of π^0 and η mesons, and the momentum constraint on the energy of isolated electrons from W and Z decays. A correction factor compensates for the imperfect containment of the shower in the cluster crystals. The absolute energy scale and residual long term drifts in the response are further corrected using $Z \to e^+e^-$ decays [25].

Interaction vertices are reconstructed from charged tracks, and the vertex of the diphoton event is taken as the one with the largest sum of squared transverse momenta (Σp_T^2) of the associated tracks. The photon four-momentum is recalculated with respect to this vertex.

Further correction factors are applied to the photon energy in order to obtain the best possible energy resolution and scale calibration, as is done in [4]. A multivariate regression technique based on simulation is used to correct the photon energy as a function of several shower shape and event variables. After applying this correction, data and simulation are compared in a sample of electrons from Z decays. Further corrections are derived using electrons from Z decays to equalize the energy scale between data and MC. Moreover, a smearing correction is applied to the simulation to match the energy resolution observed in data.

3.2 Photon selection

Photon candidates are first required to pass a sequence of filters that aim to remove beam backgrounds or identified detector issues and then to pass a preselection using more stringent criteria than the trigger requirements. The preselection is based on the shape of the electromagnetic shower in the ECAL and on the isolation energy of the photon candidate. The used variables are:

- Photon supercluster energy E_{SC}: the sum of the calibrated crystal energies;
- Preshower energy E_{SC}^{ES}: the sum of the energy deposits reconstructed in the preshower detector (ES) and associated with the supercluster;
- R_9: the energy sum of 3×3 crystals centred on the most energetic crystal in the supercluster divided by the energy of the supercluster;
- H/E: the ratio of the energy deposited in HCAL inside a cone of size $\Delta R = \sqrt{(\Delta\eta)^2 + (\Delta\phi)^2} = 0.15$ centred on the photon direction, to the supercluster energy;
- $\sigma_{\eta\eta}$: the shower transverse extension along η that is defined as:

$$\sigma_{\eta\eta}^2 = \frac{\sum (\eta_i - \bar{\eta})^2 w_i}{\sum w_i}, \tag{1}$$

where the sum runs over all elements of the 5×5 matrix around the most energetic crystal in the supercluster, and $\eta_i = 0.0174\ \hat{\eta}_i$ in EB, $\eta_i = 0.0447\ \hat{\eta}_i$ in EE with $\hat{\eta}_i$

denoting the index of the i^{th} crystal along the η direction. The individual weights w_i are given by $w_i = \max(0, 4.7 + \ln(E_i/E_{5\times5}))$, where E_i is the energy of the i^{th} crystal and $\bar{\eta} = \sum \eta_i E_i / \sum E_i$ is the weighted average pseudorapidity;

- $\text{Iso}^{0.3}_{\text{ECAL}}$ (ECAL isolation): the scalar sum of the E_{T} of the deposits in the electromagnetic calorimeter inside a cone of size ΔR = 0.3, centred on the direction of the supercluster but excluding an inner cone of size 3.5 crystals and an η-slice region of 2.5 crystals;
- $\text{Iso}^{0.3}_{\text{HCAL}}$ (hadronic calorimeter isolation): the scalar sum of the E_{T} of the deposits in the hadron calorimeter inside a hollow cone of outer radius of size $\Delta R = 0.3$ and inner radius of size $\Delta R = 0.15$ in the η-ϕ plane, centred on the direction of the supercluster;
- $\text{Iso}^{0.3}_{\text{TRK}}$ (tracker isolation): the scalar sum of the p_{T} of the tracks that are consistent with originating from the primary vertex in the event, and inside a hollow cone of outer radius of size $\Delta R = 0.3$ and inner radius of size $\Delta R = 0.04$ in the η-ϕ plane, centred around a line connecting the primary vertex with the supercluster but excluding an η-slice region ($\Delta\eta = 0.015$).

The isolation requirements are kept loose because the isolation is used as the discriminating variable in the signal extraction procedure. The selection criteria are defined to be slightly tighter than the trigger selection. The shower shape variables in the simulation are corrected to compensate for their imperfect modeling, using factors extracted from a high purity sample of photons in $\text{Z} \to \mu^+\mu^-\gamma$ events. The list of preselection criteria is presented in Table 1.

Variable	Requirement
Photon cluster + preshower energy	$E_{SC} + E^{ES}_{SC} > 20\,\text{GeV}$
H/E	if ($R_9 > 0.9$): H/E < 0.082 (EB), 0.075 (EE) if ($R_9 < 0.9$): H/E < 0.075
$\sigma_{\eta\eta}$	$0.001 < \sigma_{\eta\eta} < 0.014$ (EB), 0.034 (EE)
ECAL isolation in a ΔR=0.3 cone	$\text{Iso}^{0.3}_{\text{ECAL}} < 4\,\text{GeV}$ (only if $R_9 < 0.9$)
HCAL isolation in a ΔR=0.3 cone	$\text{Iso}^{0.3}_{\text{HCAL}} < 4\,\text{GeV}$ (only if $R_9 < 0.9$)
TRK isolation in a ΔR=0.3 cone	$\text{Iso}^{0.3}_{\text{TRK}} < 4\,\text{GeV}$ (only if $R_9 < 0.9$)

Table 1: List of requirements that a candidate photon has to satisfy to pass the analysis preselection.

The preselected photons must satisfy additional requirements to be considered as photon candidates. These consist of the absence of reconstructed electron track seeds in the pixel detector which match the candidate's direction, a tighter selection on the hadronic leakage of the shower and the $\sigma_{\eta\eta}$ shower shape variable. The list of additional selection criteria is shown in Table 2.

3.3 Jet selection

Jets are constructed by clustering particles reconstructed by the particle-flow algorithm. For this analysis, the anti-k_{T} algorithm [27] is used with a size parameter $R = 0.5$.

Jets energy corrections [28] are applied to correct the jet response to the original jet energy, both in data and simulation. The jet energy is smeared in the simulation to match the jet energy

Variable	Requirement
Matched pixel measurements	False
H/E	H/E < 0.05
$\sigma_{\eta\eta}$	$\sigma_{\eta\eta} < 0.011$ (EB), 0.030 (EE)

Table 2: List of additional requirements applied in the photon candidate selection.

resolution observed in data [28]. The jet acceptance is defined by the $p_{\mathrm{T}} > 25\,\mathrm{GeV}$, $|\eta| < 4.7$ requirements. Each jet is required to pass requirements aiming at rejecting jets coming from pileup interactions [29].

3.4 Event selection

Events containing two photons are selected by requiring two photons with a transverse momentum of at least 40 GeV and 25 GeV respectively. A minimum ΔR separation of 0.45 is required between the two photons, in order to avoid energy from the deposit of a photon to enter inside the cone considered for the isolation of the other photon.

Events are additionally required to contain at least one or two jets satisfying the criteria described in the previous paragraph, depending on the differential observable under study. Jets within a cone of $\Delta R < 1.0$ from one of the selected photon candidates are not considered.

3.5 Acceptance at generator level

In analogy with the selection requirements applied on reconstructed quantities, the fiducial phase space at particle level is defined as follows:

- Two final state photons with $p_{\mathrm{T}} > 40, 25\,\mathrm{GeV}$ respectively are required in the pseudorapidity range $|\eta| < 2.5$, $|\eta| \notin [1.44, 1.57]$. The cone isolation around each photon, calculated by summing up the transverse momenta of all final state particles in a cone $\Delta R < 0.4$ centred on the photon, is required to be less than 5 GeV. The separation between the two photons is required to be $\Delta R > 0.45$.
- At least one or two jets are required (depending on the differential observable under study), clustered with the anti-k_{T} algorithm with a size parameter $R = 0.5$ from the set of final state particles (including neutrinos). The jets are required to have a transverse momentum of at least 25 GeV and a pseudorapidity $|\eta| < 4.7$, and to have a distance $\Delta R > 1.0$ from each of the selected photons.

The results of the cross section measurement refer to the phase space defined by these requirements.

4 Signal yield determination

The number of events where two prompt photons are produced and pass the selection is measured by extracting their purity among the events passing the full event selection. This is needed to quantify the fraction of events where at least one of the reconstructed photons is indeed a jet, or $Z \to ee$ events where both electrons pass the pixel veto requirement. The signal fraction is extracted in each bin of the observables under study through a binned maximum likelihood fit.

4.1 Particle flow isolation

Among the different components (charged, neutral, photon) of the PF isolation, the photon one is observed to have the smallest correlation with the electromagnetic shower shape. As it will be explained in Section 4.2, this is a key ingredient of the analysis. The photon component is computed in a cone of size ΔR = 0.4 around each selected photon candidate, as the E_{T} scalar sum of photons reconstructed with the PF algorithm. The PF isolation is better quantified in cases of overlapping particles than the calorimetry-based isolation.

Because the photon energy can leak into the isolation cone biasing the isolation sum, the energy deposited by the selected photon candidate is subtracted by removing the area where the photon is expected to have deposited its energy ("footprint"). This procedure is applied on an event-by-event basis relying on simple geometrical considerations. The directions of the momenta of photons entering the isolation cone around the selected photon candidate are extrapolated up to the inner surface of the ECAL, and whenever they overlap with a crystal belonging to the supercluster associated with the selected photon candidate they are removed from the isolation sum.

The energy flow from overlapping pp interactions in the same LHC bunch crossing (pileup) introduces a spurious correlation between the two candidate photons' isolation sums. For this reason the PF isolation sums for both photons are corrected, event by event, for the presence of pileup with a factor proportional to the average pileup energy density (ρ) calculated with FASTJET [30]. Because of this, the isolation can assume values below zero.

4.2 Template construction

The diphoton signal is extracted through a two-dimensional binned maximum likelihood fit that uses the isolation of the two selected photon candidates as discriminating variables. Different templates are built for the prompt-prompt (f_{pp}), prompt-non-prompt (f_{pn}), non-prompt-prompt (f_{np}), and non-prompt-non-prompt (f_{nn}) components in the (Iso_1,Iso_2) plane, where Iso_1 and Iso_2 represent the isolation variables for the two selected photon candidates in the event. The probability distribution function has the following form:

$$\begin{aligned}\mathcal{P}_{2D}(\mathrm{Iso}_1, \mathrm{Iso}_2) = f_{pp} \cdot T_{pp}(\mathrm{Iso}_1, \mathrm{Iso}_2) + f_{pn} \cdot T_{pn}(\mathrm{Iso}_1, \mathrm{Iso}_2) \\ + f_{np} \cdot T_{np}(\mathrm{Iso}_1, \mathrm{Iso}_2) + f_{nn} \cdot T_{nn}(\mathrm{Iso}_1, \mathrm{Iso}_2)\end{aligned} \tag{2}$$

where $T_{kk}(\mathrm{Iso}_1, \mathrm{Iso}_2)$ is the probability distribution function describing simultaneously the isolation distribution (template) for the component f_{kk}. Techniques have been developed to extract the templates from data to avoid possible biases coming from an imperfect modeling of the events in the simulation. Samples of events where at least one photon passes the photon selection are used to create prompt-prompt, prompt-non-prompt, non-prompt-prompt and non-prompt-non-prompt templates with high statistical precision, as described below.

The "random cone" technique is used to model the isolation of prompt photons with high statistical accuracy. In this procedure we compute the isolation energy in a region separated from the photon. Starting from the photon (η, ϕ) axis, a new axis is defined at the same pseudorapidity η but with a random separation in azimuthal angle ϕ_{RC} between 0.8 and $2\pi - 0.8$ radians from the photon ϕ. This new axis is used to define the random cone provided that no jet with $p_{\mathrm{T}} > 20\,\mathrm{GeV}$ or photon or electron with $p_{\mathrm{T}} > 10\,\mathrm{GeV}$ is reconstructed within $\Delta R < 0.8$ and no muon is reconstructed within $\Delta R < 0.4$ from this axis. In the case where the new axis does not meet these requirements, a new azimuthal angle is generated. The isolation energy, which is defined as the energy collected in a cone of size $\Delta R < 0.4$ about the new axis once the fraction

corresponding to the area of the photon supercluster has been removed, is then used to populate the prompt photon template. The isolation distribution of electrons in $Z \to e^+e^-$ events has been studied and found to agree with the results of the random cone technique.

The isolation of background (non-prompt) photons cannot be modeled by simply inverting the photon preselection, because the candidates entering the analysis, i.e. fulfilling the preselection requirements, have "photon-like" characteristics, while the set of candidates not fulfilling the photon preselection criteria includes a large number of genuine jets. To avoid this bias, the candidates selected to model the isolation of non-prompt photons are chosen from those that fulfil all the photon selection criteria, except the $\sigma_{\eta\eta}$ shower shape, which is not strongly correlated with the isolation variable as a result of the footprint removal technique described in the previous Section. The events in a "sideband" close to the photon selection criterion are used to populate the non-prompt photon template. The sideband is defined as $0.011 < \sigma_{\eta\eta} < 0.014$ for candidates reconstructed in the ECAL barrel and $0.030 < \sigma_{\eta\eta} < 0.034$ for candidates reconstructed in the ECAL endcaps.

The same procedure illustrated in Section 4.1 is used for subtracting the pileup energy from the photon isolation. The templates obtained using the random cone and the sideband techniques in the simulation are compared with the one-dimensional PF isolation distribution for prompt and non-prompt photons in simulated events and with the templates obtained from data (Figs. 1 and 2). The residual differences in the simulation between the isolation distribution and the templates defined with the random cone and the sideband techniques are accounted for as systematic uncertainties on the template shapes.

The two-dimensional templates $(\mathrm{Iso}_1, \mathrm{Iso}_2)$ are constructed from data by selecting photon events with similar characteristics to those of the diphoton events to be fitted. The procedure presented below correctly models the isolation distribution even in the case of overlap between the isolation cones of the two photon candidates.

The prompt-prompt template is built from events with at least one photon candidate where the pileup energy density matches that of the event to be fitted, and where the two random cone directions are found having the same pseudorapidity and the same azimuthal angular separation as the selected photons.

The prompt-non-prompt template is built from events where a sideband photon is selected. The isolation sum around the sideband photon is used for the candidate to be fitted under the non-prompt-hypothesis. A direction corresponding to the one of the second candidate in the selected diphoton event is used to calculate the isolation sum for the candidate to be fitted under the prompt hypothesis.

The non-prompt-non-prompt template is built selecting two events, each of which contains one sideband photon and such that their orientation matches the orientation of the candidate photons in the event to be fitted. Then, depending on the fraction of photon candidates with $\Delta R_{\gamma\gamma} < 1.0$ present in the bin of the observable under analysis, a choice between two different strategies is made. If the fraction is below 10%, the effect of the overlapping isolation cones can be neglected. The two-dimensional non-prompt-non-prompt template is then built by calculating each of the two isolation sums in the separate events. If the fraction is above 10%, an additional requirement is imposed: the sum of the FastJet ρ of the two selected template events has to match the one of the diphoton event to be fitted. Then, the sets of reconstructed particles in the two template events are merged, and the isolation sums are calculated from this merged set of reconstructed particles along the direction of each sideband photon.

In this procedure, the pileup energy density of the template events is used to model the pileup

energy density of the event to be fitted, and this allows us to describe the correlation between the isolation sums. The effect of the residual correlation mis-modeling is added to the template shape systematic uncertainty in the final result.

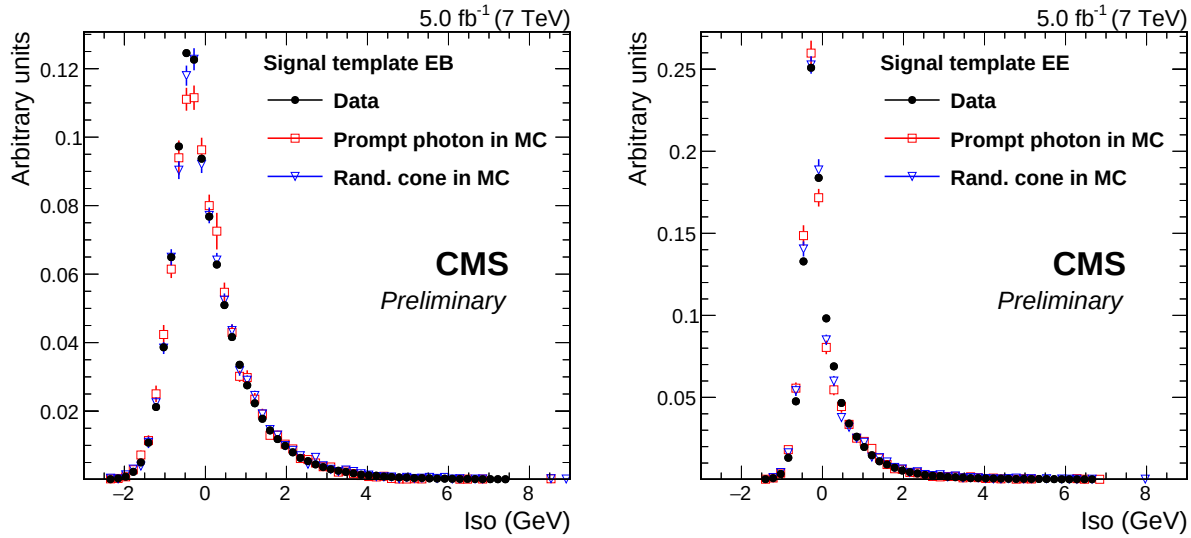

Figure 1: Comparison of prompt photon templates in data and simulation: (red) prompt photons in the simulation, (blue) prompt photon templates extracted with the random cone technique from simulation and (black) from data; *Left:* photon candidates in the ECAL barrel, *Right:* photon candidates in the ECAL endcaps. All histograms are normalized to unit area.

4.3 Fitting technique

The fit is performed separately for the cases where both photon candidates are reconstructed in the ECAL barrel, one in the ECAL barrel and one in the ECAL endcaps, or both in the ECAL endcaps. The extracted yields are then added up. If both photon candidates are in the same detector region (EB-EB and EE-EE categories), the leading photon is assigned randomly to axis 1 or 2 of the two-dimensional plane, and the prompt-non-prompt (f_{pn}) and non-prompt-prompt (f_{np}) fractions are constrained to have the same value.

The fit, performed in each bin of the differential variables, is restricted to the region where the isolation of the photons is smaller than 9 GeV (this requirement is applied in addition to those described in Section 3.2). To guarantee its stability even in the less populated bins, the fit is performed in steps. First the size of the bins in the two-dimensional plane $(\mathrm{Iso}_1, \mathrm{Iso}_2)$ is optimised to reduce statistical fluctuations of template shape in the tails; then a first fit is performed on the projections of the isolation distributions on the two axes of the plane using the one-dimensional templates described above. In a subsequent step, the fractions of prompt-prompt, prompt-non-prompt, non-prompt-prompt, and non-prompt-non-prompt, which are constrained to sum up to unity, are fit in the two-dimensional plane using as a constraint the results of the previous fit. The final likelihood maximisation is then performed after removing all constraints, and using as initial values of the parameters those found in the previous step.

In events with at least one jet in the final state, the cross section is measured as a function of the number of jets in the final state ($\mathrm{N_{jets}}$), the ΔR separation between the leading jet and the leading ($\Delta R^{lead}_{\gamma,j}$) and sub-leading ($\Delta R^{trail}_{\gamma,j}$) photon respectively, the minimum ($\Delta R^{close}_{\gamma,j}$) and maximum ($\Delta R^{far}_{\gamma,j}$) ΔR separation between the leading jet and the two leading photons, and the transverse momentum of the leading jet ($p_{T,j}$).

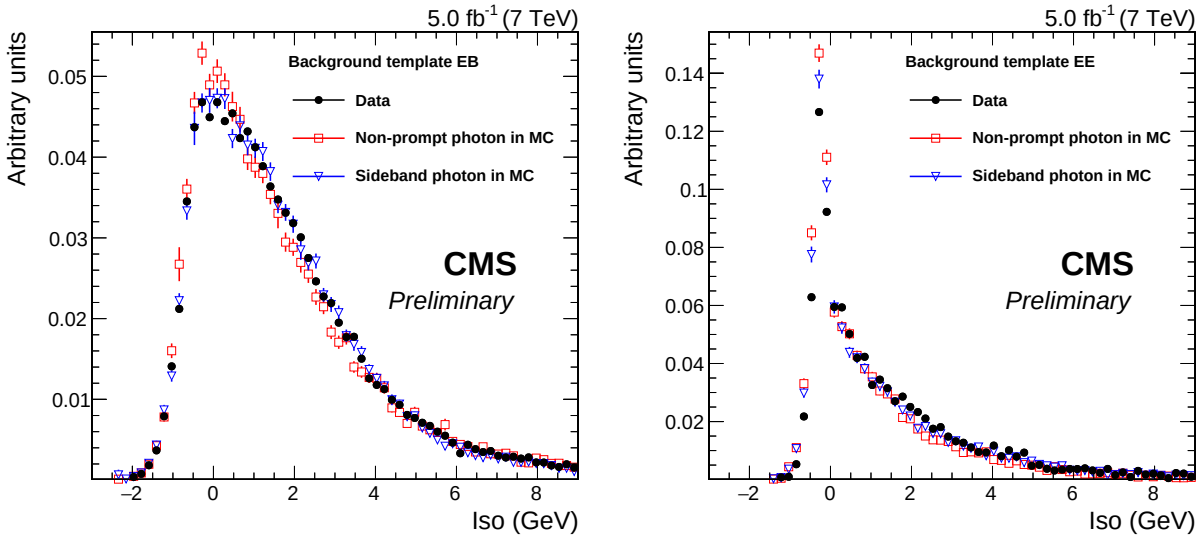

Figure 2: Comparison of non-prompt photon templates in data and simulation: (red) non-prompt photons in the simulation, (blue) non-prompt photon templates extracted with the sideband technique from simulation and (black) from data; *Left:* candidates in the ECAL barrel, *Right:* candidates in the ECAL endcaps. All histograms are normalized to unit area.

In events with at least two jets in the final state, the cross section is measured as a function of the transverse momenta, invariant mass, ΔR, $\Delta\eta$ and $\Delta\phi$ separation of the two leading jets ($p_{T,j}^{lead}$, $p_{T,j}^{trail}$, m_{jj}, ΔR_{jj}, $\Delta\eta_{jj}$, $\Delta\phi_{jj}$), the $\Delta\phi$ separation between the systems composed by the two leading photons and two leading jets ($\Delta\phi_{\gamma\gamma,jj}$), and the Zeppenfeld variable [31] ($|y_{\gamma\gamma} - (y_{j_1} + y_{j_2})/2|$) of the event . These variables are especially motivated by their use to discriminate VBF-produced Higgs events from the diphoton QCD background.

The fractions of prompt-prompt, prompt-non-prompt, and non-prompt-non-prompt components are shown in Fig. 3 for some of the observables listed above. The reported purity suffers from a contamination of electrons coming predominantly from Drell-Yan $e^+e^-$and incorrectly reconstructed as photons. The contamination is most significant in the Z peak region, where it reaches about 7% of the total yield. The fraction of electron pairs passing the analysis selection and contributing to the prompt-prompt fitted fraction is estimated from simulation, where correction factors are applied to obtain the electron to photon mis-identification probability measured in data.

5 Efficiencies and unfolding

Following the methodology presented in the previous sections, the yield of diphoton events after selection is extracted. To obtain the final result, this cross section is corrected for inefficiencies and unfolded from the measured quantities to the corresponding particle-level quantities.

The total diphoton efficiency can be separated into trigger efficiency and reconstruction/selection efficiency, and can be written as:

$$\epsilon_{\gamma\gamma} = \epsilon_{\text{trig}} \times \epsilon_{\text{sel}} \times C_{\gamma 1}^{Z\to e^+e^-} \times C_{\gamma 2}^{Z\to e^+e^-} \times C_{\gamma 1}^{Z\to \mu^+\mu^-\gamma} \times C_{\gamma 2}^{Z\to \mu^+\mu^-\gamma}, \quad (3)$$

where ϵ_{trig} is the trigger efficiency and ϵ_{sel} is the diphoton reconstruction/selection efficiency from simulation. The factors $C_{\gamma 1}^{Z\to e^+e^-}$ and $C_{\gamma 2}^{Z\to e^+e^-}$ are the corrections to the efficiency for each

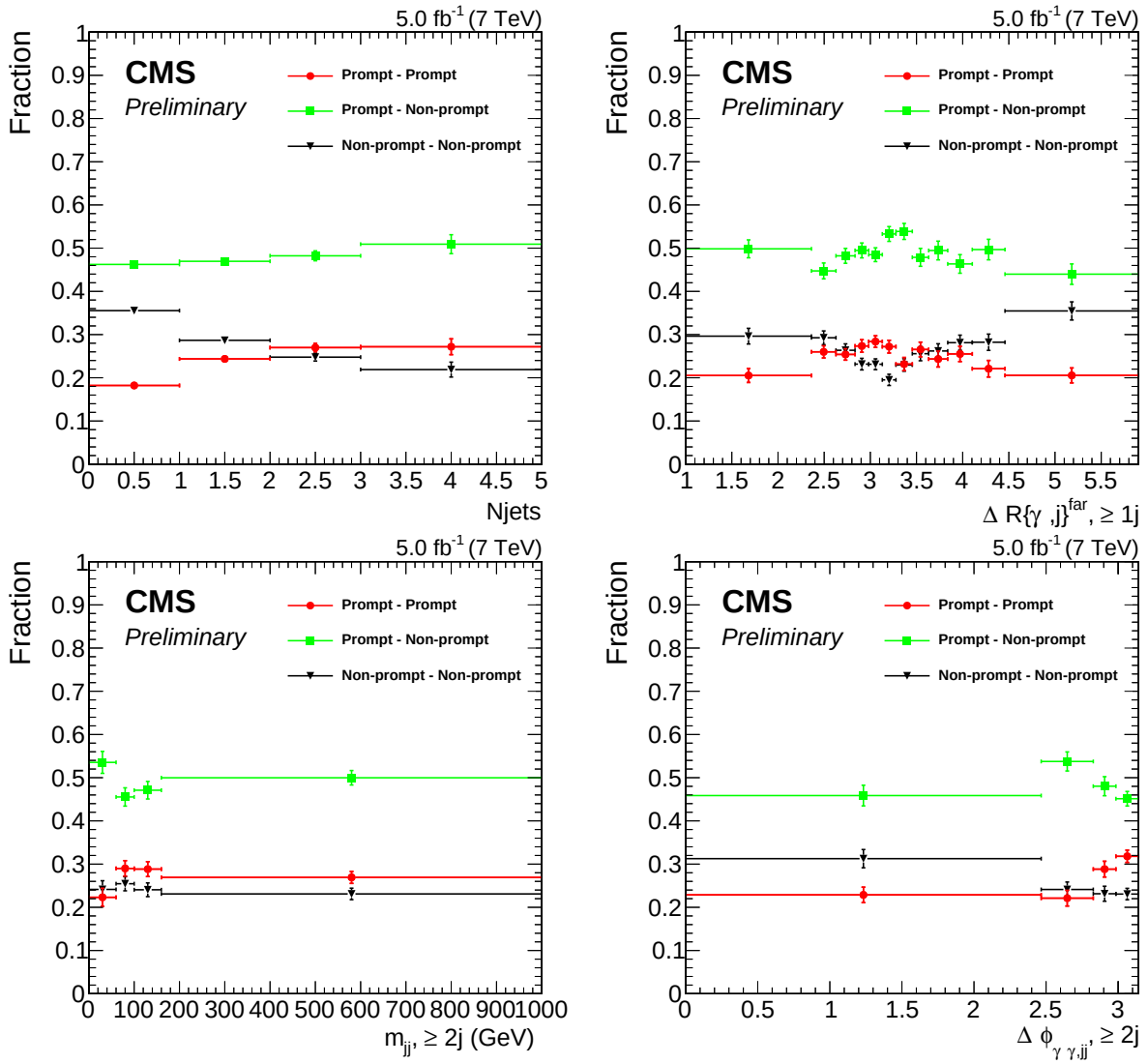

Figure 3: Fractions of prompt-prompt, prompt-non-prompt and non-prompt-non-prompt components as a function of the differential variables. Uncertainties are statistical only. The differential variable under study is indicated on the horizontal axis label.

photon candidate to pass all the selection requirements except the electron veto; $C_{\gamma 1}^{Z\to\mu^+\mu^-\gamma}$ and $C_{\gamma 2}^{Z\to\mu^+\mu^-\gamma}$ are the corrections to the electron veto efficiency.

The values of the correction factors are determined from the ratio of the efficiency in data to those in the simulation, measured with a tag-and-probe method using (i) samples of $Z \to e^+e^-$ for the full selection except the electron-veto requirement, and (ii) samples of photons from the final-state-radiation of $Z \to \mu^+\mu^-\gamma$ for the electron-veto requirement.

The diphoton reconstruction/selection efficiency ϵ_{sel} is evaluated differentially as a function of each differential variable, and amounts inclusively to about 70%. All the efficiency correction factors are studied as a function of the photon E_{T} and η and found to be compatible with unity to within 2%.

The unfolding procedure is performed with the iterative D'Agostini method [32] using the RooUnfold [33] software package. The unfolding response model is built using SHERPA simulated events. Monte Carlo pseudo-experiments are used to estimate the statistical uncertainty in the unfolded results.

6 Systematic uncertainties

Table 3 summarises the main sources of systematic uncertainty in the measurement of the diphoton cross section.

The dominant uncertainty in the prompt diphoton purity stems from the uncertainty in the modeling of the template variable. We estimate this uncertainty by comparing fit results obtained using the templates built with the techniques described in Section 4 with those obtained using the distributions of the isolation variable for prompt or non-prompt isolated photons in simulated events. The latter are used to generate data samples for each bin of the differential variables, with the fractions measured in data. Then, each of these datasets is fitted with templates built in the simulation with the same techniques used on data, and the average difference between the fitted fractions and those used for the generation is quoted as a systematic uncertainty. It amounts to 3% (barrel template) and 4% (endcap template) for the prompt component, and between 6% (barrel template) and 9% (endcap template) for the non-prompt component. The uncertainty in the template shape for fragmentation photons is evaluated in the simulation by doubling the probability of the fragmentation process, yielding an additional 1.5% uncertainty in the measured cross section. In the case of the non-prompt-non-prompt template, and only for the bins where a significant fraction of the diphoton candidates are close in $\Delta R_{\gamma\gamma}$, an additional uncertainty ranging from 3% to 5% is introduced to account for the imperfections on the template shape description due to the effect of ECAL noise and PF thresholds on the combination of two different events to build the template.

The systematic uncertainty arising from the statistical uncertainty in the shape of the templates is evaluated generating modified templates, where the content of each bin is represented by a Gaussian distribution centred on the nominal bin value and with standard deviation equal to the statistical uncertainty of the bin. The root mean square of the distribution of the fitted purity values, divided by the purity measured with the original template, is used as systematic uncertainty in the purity measurement and amounts to about 3%.

A possible bias associated with the fitting procedure is evaluated using pseudo-experiments. Pseudo-data samples are generated with given fractions of prompt-prompt, prompt-non-prompt, and non-prompt-non-prompt contributions, using the templates from simulation as generator

Table 3: Main sources of systematic uncertainty in the diphoton cross section. The values reported are the typical ones.

Source of uncertainty	
Prompt template shape (EB)	3%
Prompt template shape (EE)	4%
Non-prompt template shape (EB)	6%
Non-prompt template shape (EE)	9%
Effect of fragmentation component	1.5%
Template statistical fluctuation	3%
Jet energy scale and resolution	3-15%
Pileup description	1.5%
Unfolding response model	5%
Integrated luminosity	2.2%

probability density functions. Each data sample is then fitted with the same templates used for the generation. The average bias is negligible in all bins.

Uncertainties on the jet observables arise from the imperfect description of the jet energy scale and resolution and of the pileup. For the case of the jet energy scale and resolution, the uncertainties associated with the correction factors are propagated to the measured cross section, and range from 3% to 15% depending on the differential variable under study. The uncertainty from the pileup description is about 1.5%.

The pileup uncertainty is estimated by re-calculating the distribution of the number of overlapping proton-proton interactions under the assumption of a total inelastic cross section varied by $\pm 5\%$ with respect to its nominal value. This modified distribution is used for reweighting the simulated events, and the change in the measured cross section induced by this change is quoted as a systematic uncertainty.

The systematic uncertainty associated with the unfolding model is evaluated from the results obtained using an alternative response model from MADGRAPH +PYTHIA. They typically differ by about $\sim$ 5% from the nominal ones obtained with the SHERPA model. The statistical uncertainty in the response model is negligible.

The systematic uncertainty associated with the subtraction of Drell-Yan e^+e^- events is evaluated by propagating the uncertainty in the electron to photon mis-identification probability to the subtracted yield. The uncertainty in the fraction of such events that is fitted as prompt-prompt is also taken into account. Both contributions are below 1% of the integrated diphoton cross section.

The systematic uncertainty in the trigger efficiency is found to be below 0.5%. The systematic uncertainty in the reconstruction and selection efficiencies is obtained from the uncertainty in the data-to-simulation corrections from the $Z \to e^+e^-$ and $Z \to \mu^+\mu^-\gamma$ control samples.

The systematic uncertainty in the integrated luminosity that corresponds to our data sample is 2.2% [34].

7 Results and comparison with theoretical predictions

Diphoton production in association with jets has been calculated at next-to-leading order by the GoSam [35], BlackHat [36] and NJET [37] Collaborations. The measured cross section at particle level is compared here to predictions obtained using the SHERPA [18], aMC@NLO [38]

and GoSam event generators.

SHERPA includes the Born contribution with up to three additional real emissions in the final state, and the box contribution at matrix element level. The fragmentation process of quark and gluon to photon is treated as photon emission from the additional jets. Hadronization is also performed within the same generator. The CT10 PDF set has been used. The factorization scale has been set to the internal SHERPA-METS scale, corresponding to the lowest invariant mass or negative virtuality in the core 2→2 configuration clustered using a k_T-type algorithm. SHERPA has been shown to agree very well with data on the distribution of differential observables for inclusive diphoton production [7]. The referenced measurement suggests that SHERPA underestimates the inclusive diphoton production cross section by about 20%.

The aMC@NLO event generator describes the diphoton production in association with up to 2 jets at NLO. The FxFx merging technique [39] is used to merge different jet multiplicities. Events are generated using the NNPDF 3.0 NLO PDF set [40], and hadronized with PYTHIA 8 [41] using the CUETP8M1 tune. The PDF uncertainty is evaluated as the rms of the predictions obtained with all NNPDF set replicas. The aMC@NLO prediction is complemented by the box diagram contribution calculated with PYTHIA 8.

The parton-level GoSam prediction describes the diphoton production in association with at least one or two jets at NLO. The predictions for the 1-jet and 2-jet selections are provided separately. Therefore, GoSam cannot be used to predict the cross section as a function of jet multiplicity. The GoSam prediction is corrected for the fact that it does not include parton shower or underlying event contribution. The fraction of events not selected due to underlying hadronic activity is estimated using the PYTHIA 8 event generator with tunes CUETP8M1 and 4C [42]. A correction factor of 0.95 ± 0.05 is applied to the predicted cross section.

For all generators, the scale uncertainty is evaluated by varying the factorization and renormalization scales up and down by a factor of 2.

The integrated cross sections measured in data for the 1-jet and 2-jet selections are:

$$\sigma_{data}^{1-jet} = 7.4 \pm 0.2\ (\text{stat.}) \pm 1.0\ (\text{syst.}) \pm 0.2\ (\text{lumi})\ \text{pb}$$

$$\sigma_{data}^{2-jet} = 2.3 \pm 0.1\ (\text{stat.}) \pm 0.4\ (\text{syst.}) \pm 0.1\ (\text{lumi})\ \text{pb}$$

compared with:

$$\sigma_{\text{SHERPA}}^{1-jet} = 5.9^{+1.9}_{-1.3}\ (\text{scale+stat.})\ \text{pb}$$

$$\sigma_{a\text{MC@NLO}}^{1-jet} = 8.3^{+1.2}_{-1.2}\ (\text{scale+pdf+stat.})\ \text{pb}$$

$$\sigma_{\text{GoSam}}^{1-jet} = 5.8^{+0.9}_{-0.8}\ (\text{scale+stat.})\ \text{pb}$$

$$\sigma_{\text{SHERPA}}^{2-jet} = 1.7^{+0.8}_{-0.5}\ (\text{scale+stat.})\ \text{pb}$$

$$\sigma_{a\text{MC@NLO}}^{2-jet} = 2.5^{+0.4}_{-0.4}\ (\text{scale+pdf+stat.})\ \text{pb}$$

$$\sigma_{\text{GoSam}}^{2-jet} = 1.9^{+0.4}_{-0.4}\ (\text{scale+stat.})\ \text{pb}$$

Figures 4-10 show the shape comparisons of the differential cross sections between data and the theoretical predictions. All distributions are normalized to unitary area.

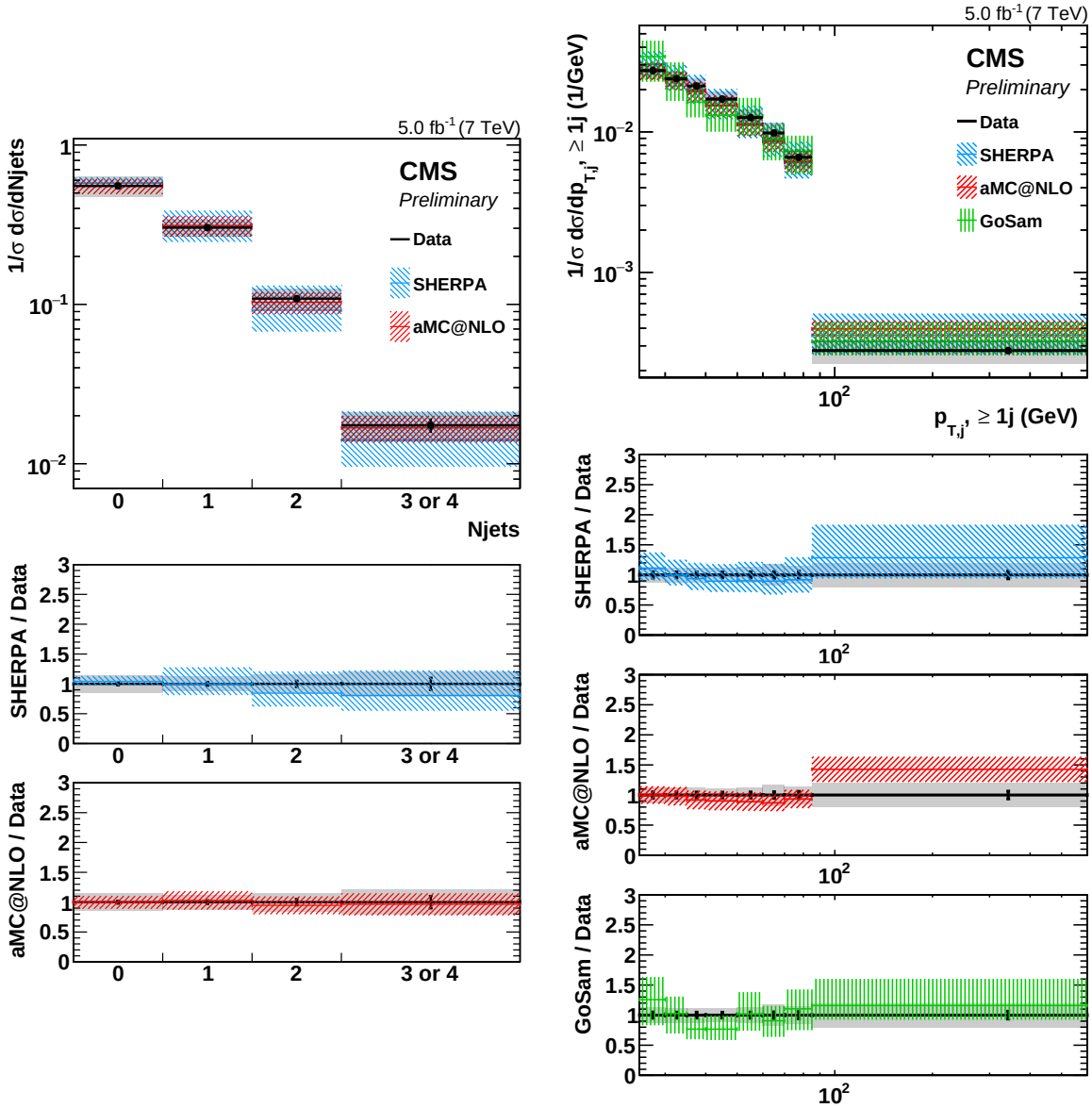

Figure 4: Comparison of the differential cross sections between data and the theoretical predictions, as a function of the exclusive number of jets (left) and jet transverse momentum (right). All distributions are normalized to unitary area.

As expected, aMC@NLO is in general less affected by the scale uncertainty with respect to SHERPA, that is a leading-order generator. The aMC@NLO prediction for the jet multiplicity is in excellent agreement with data, even for events with three jets or more. SHERPA also agrees with data within the uncertainties, but tends to under-predict the cross section in events with at least two jets.

SHERPA and aMC@NLO are in agreement with data for the jet spectrum and for the angular observables in 1-jet events. GoSam is not able to predict the angular observables to a similar level of agreement. It should be considered that GoSam is a fixed-order parton-level generator that does not account for additional jet emissions and hadronization.

SHERPA and aMC@NLO also agree with data for all observables studied in 2-jet events. GoSam is in agreement with data, with the exception of $\Delta\phi_{\gamma\gamma,jj}$ where it shows a steeper distribution.

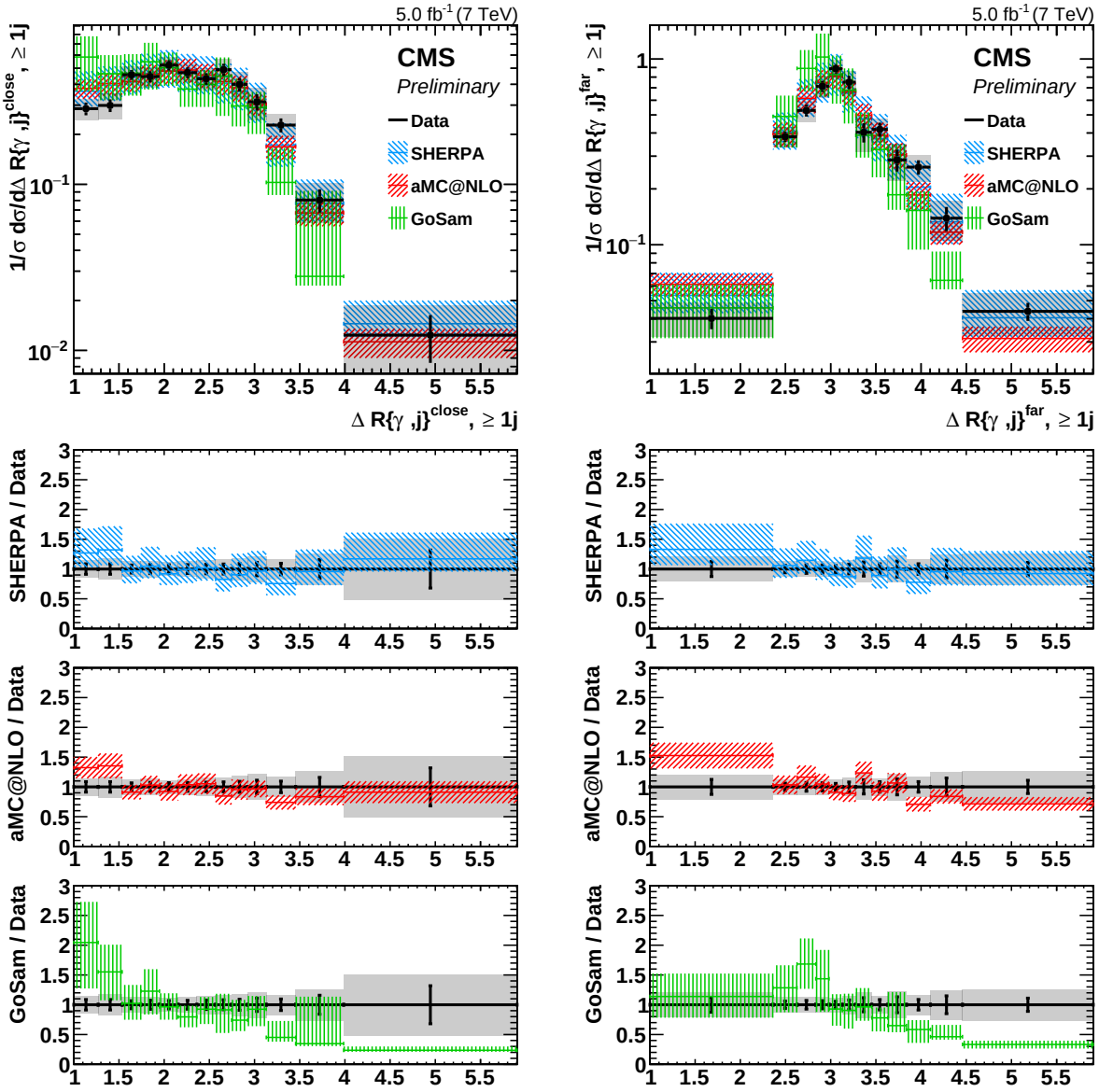

Figure 5: Comparison of the differential cross sections between data and the theoretical predictions, as a function of the ΔR separation between the leading jet and the closer (left) or more distant (right) photon. All distributions are normalized to unitary area.

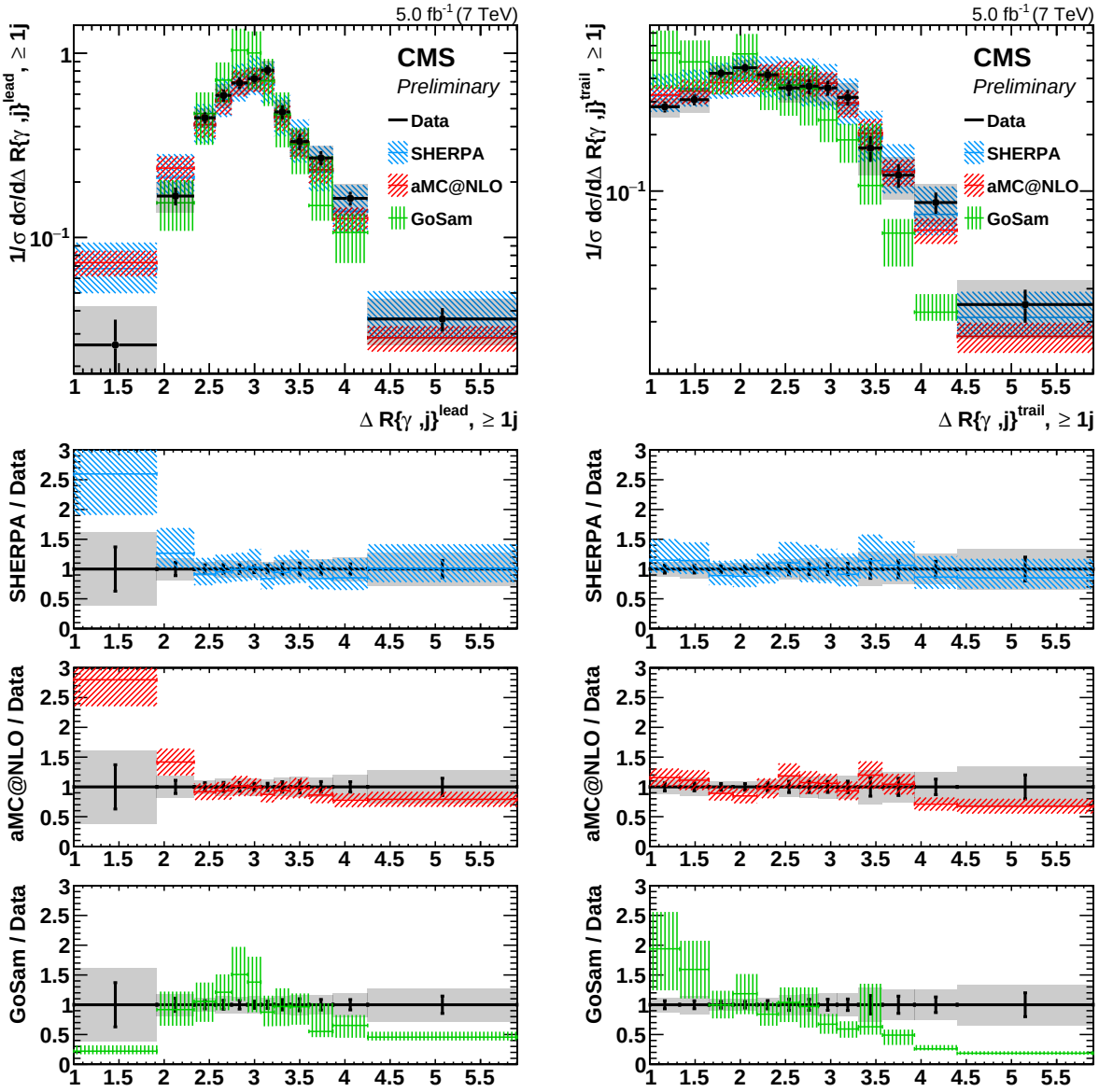

Figure 6: Comparison of the differential cross sections between data and the theoretical predictions, as a function of the ΔR separation between the leading jet and the leading (left) or subleading (right) photon. All distributions are normalized to unitary area.

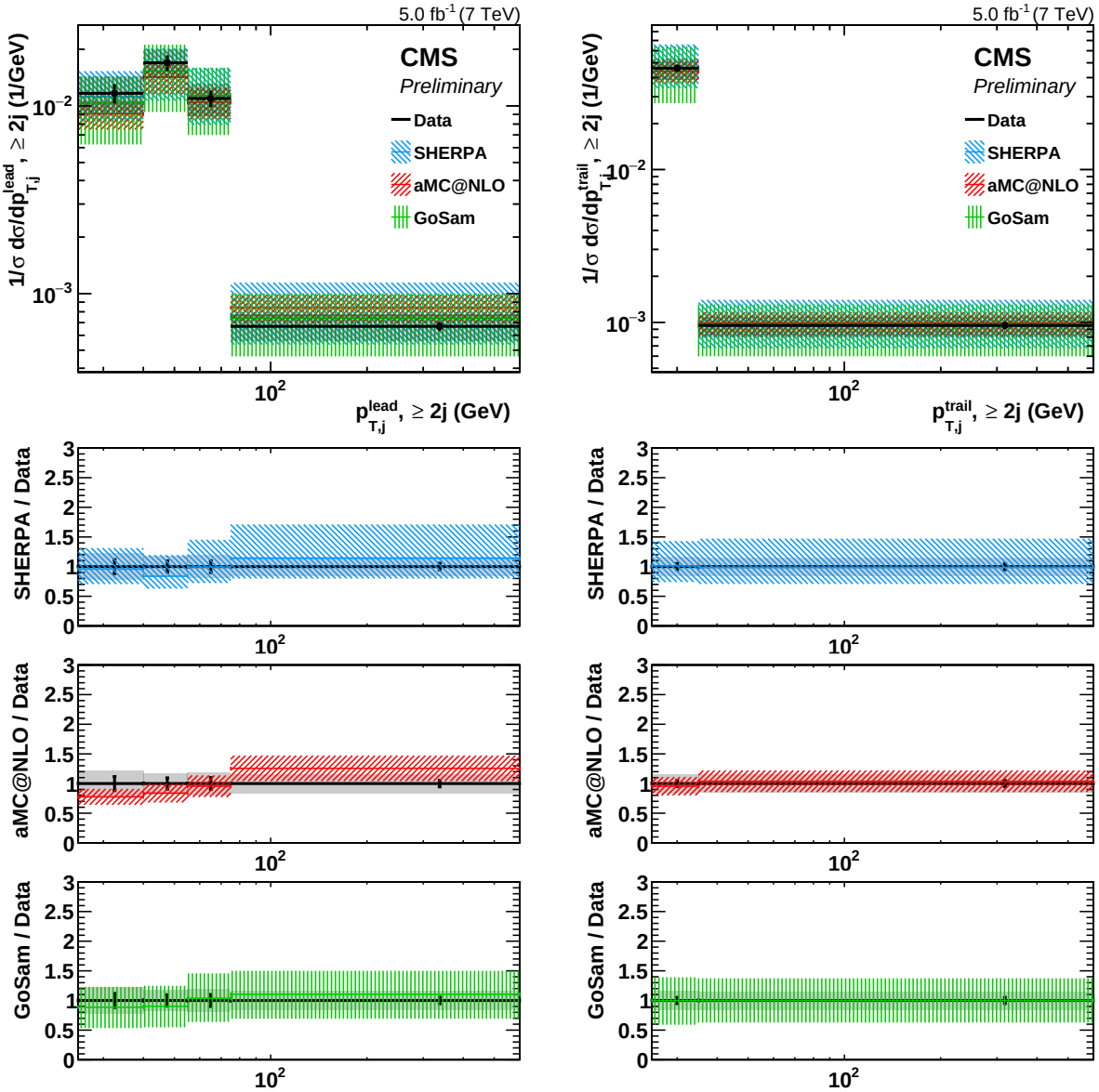

Figure 7: Comparison of the differential cross sections between data and the theoretical predictions, as a function of the leading (left) and subleading (right) jet transverse momentum. All distributions are normalized to unitary area.

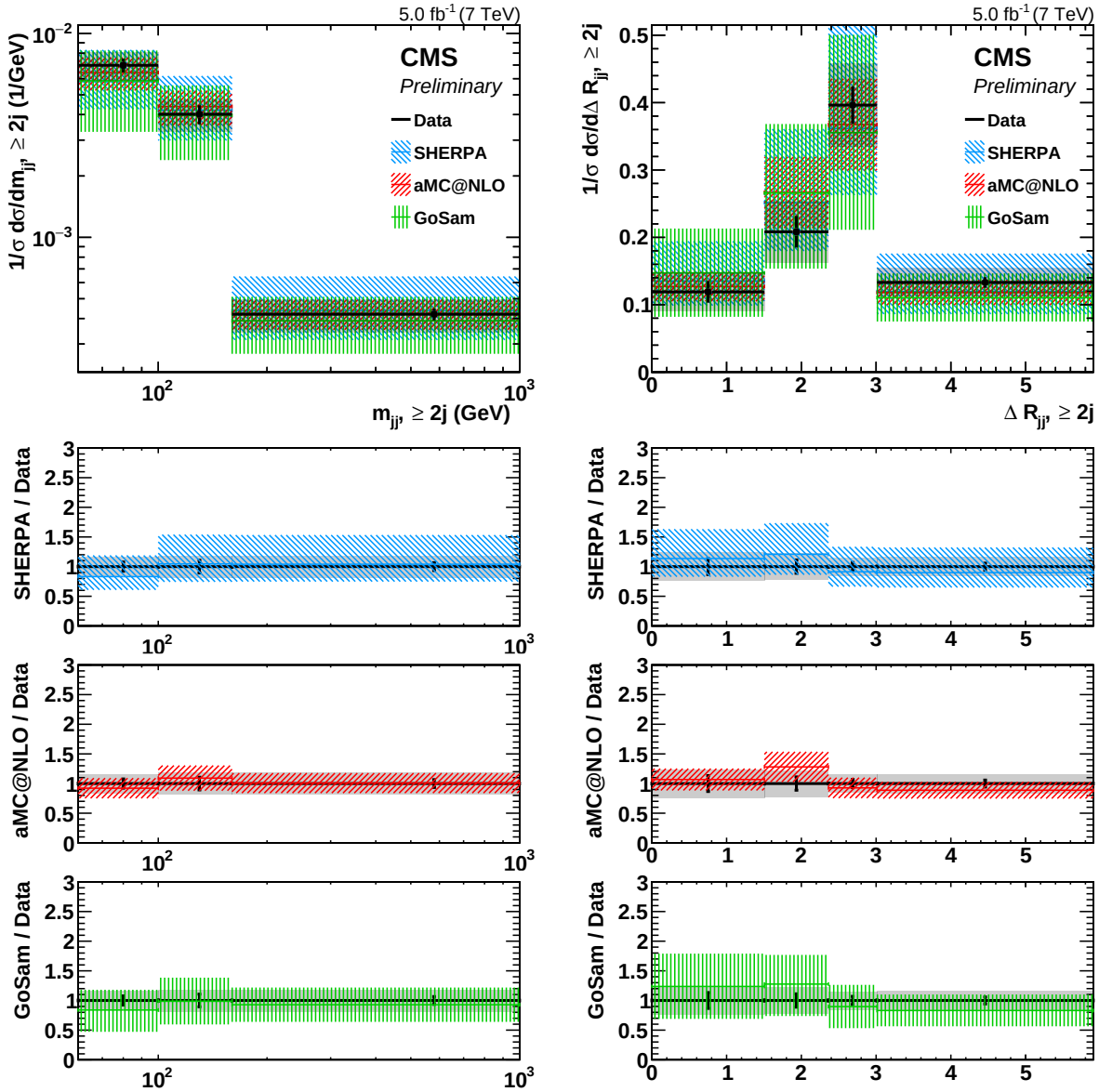

Figure 8: Comparison of the differential cross sections between data and the theoretical predictions, as a function of the di-jet invariant mass (left) and ΔR separation (right). All distributions are normalized to unitary area.

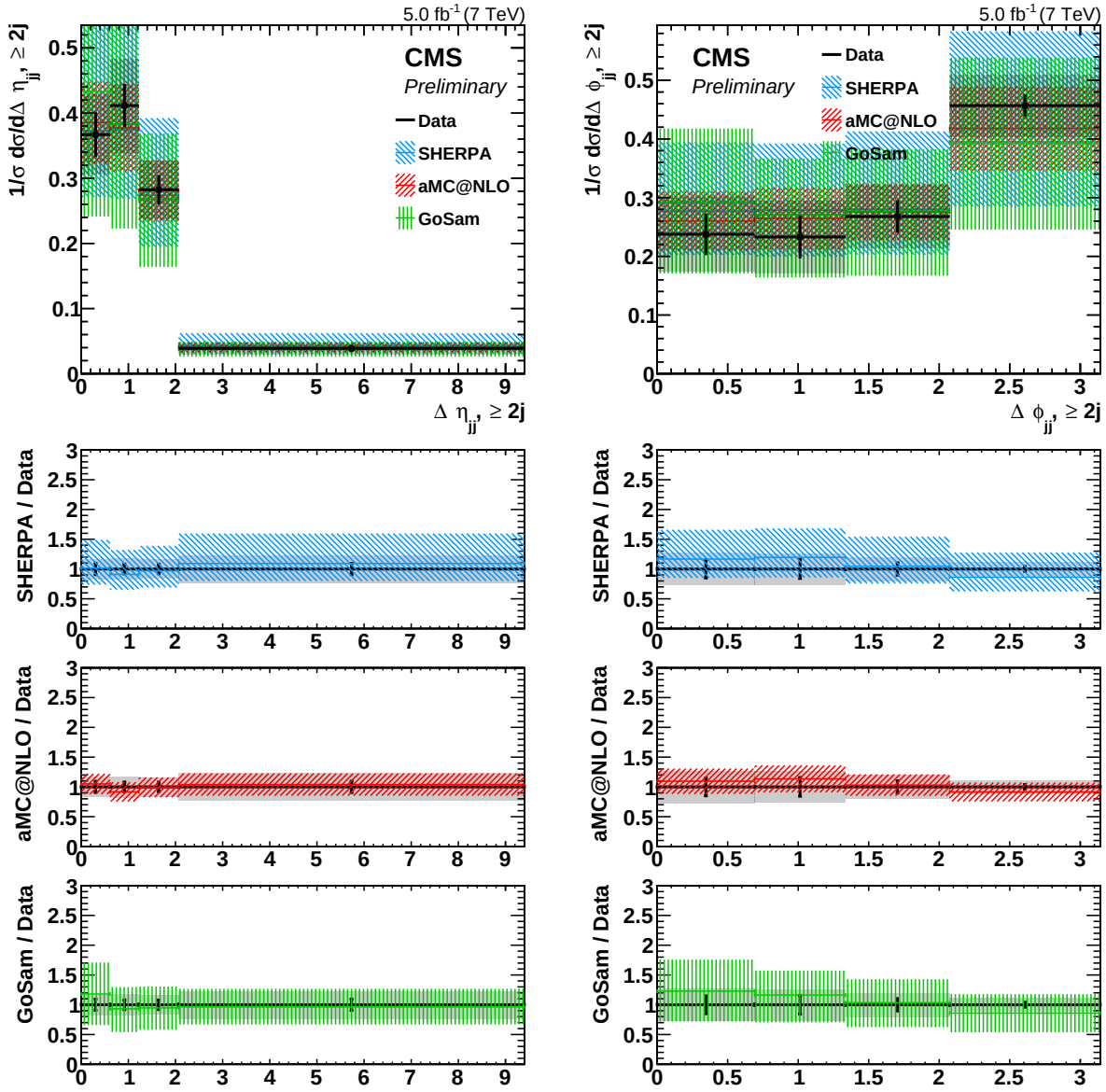

Figure 9: Comparison of the differential cross sections between data and the theoretical predictions, as a function of the $\Delta\eta$ (left) and $\Delta\phi$ (right) between the two leading jets. All distributions are normalized to unitary area.

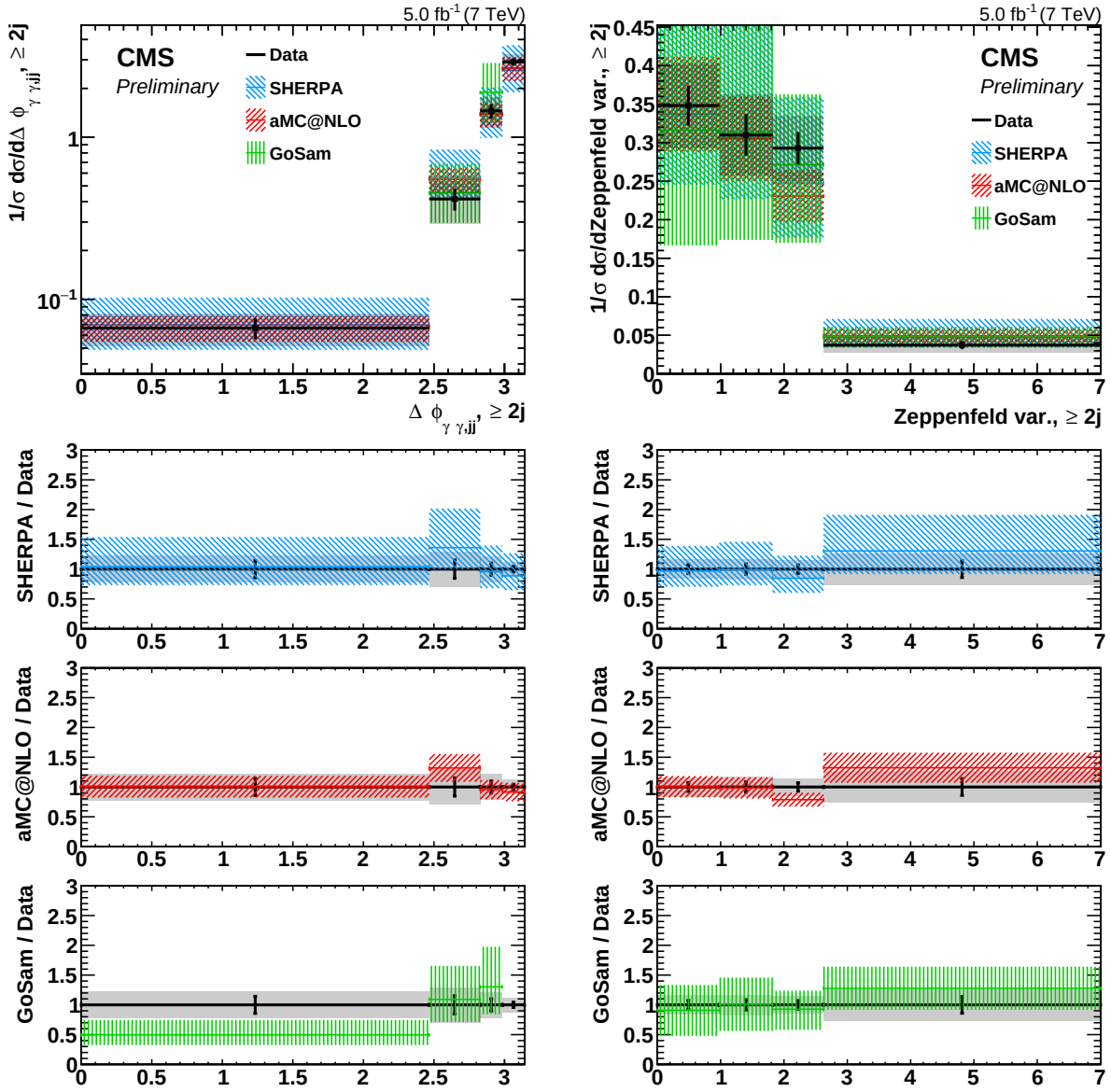

Figure 10: Comparison of the differential cross sections between data and the theoretical predictions, as a function of the $\Delta\phi$ separation between the diphoton and dijet systems (left), and the Zeppenfeld event variable (right). All distributions are normalized to unitary area. In the left plot, the GoSam prediction is normalized excluding the last bin.

8 Summary

The measurement of the differential cross sections for the production of a photon pair in association with jets in pp collisions at $\sqrt{s} = 7$ TeV has been presented. The data sample corresponds to an integrated luminosity of 5.0 fb^{-1} recorded in 2011 with the CMS detector.

A data-driven method based on the photon component of the particle flow isolation has been used to extract the prompt diphoton yield. The isolation is calculated so that the energy leakage from the photon deposit inside the isolation cone is effectively subtracted.

The cross section is measured differentially as a function of photon and jet observables in events with at least one or two hard jets in the final state. The SHERPA and aMC@NLO predictions agree with the data for a large set of differential observables, including jet multiplicity, jet spectra, angular distributions and event variables commonly used for selecting VBF production processes. The parton-level GoSam prediction also describes the data well except for the angular correlations between photons and jets, where discrepancies are observed.

References

[1] S. Catani et al., "Diphoton production at hadron colliders: a fully-differential QCD calculation at NNLO", *Phys. Rev. Lett.* **108** (2012) 072001, doi:10.1103/PhysRevLett.108.072001, arXiv:1110.2375.

[2] ATLAS Collaboration, "Observation of a new particle in the search for the Standard Model Higgs boson with the ATLAS detector at the LHC", *Phys. Lett. B* **716** (2012) 1, doi:10.1016/j.physletb.2012.08.020, arXiv:1207.7214.

[3] CMS Collaboration, "Observation of a new boson at a mass of 125 GeV with the CMS experiment at the LHC", *Phys. Lett. B* **716** (2012) 30, doi:10.1016/j.physletb.2012.08.021, arXiv:1207.7235.

[4] CMS Collaboration, "Observation of the diphoton decay of the Higgs boson and measurement of its properties", *Eur.Phys.J.* **C74** (2014), no. 10, 3076, doi:10.1140/epjc/s10052-014-3076-z, arXiv:1407.0558.

[5] J. T. Ruderman and D. Shih, "General neutralino NLSPs at the early LHC", *J. High Ener. Phys.* **08** (2012) 159, doi:10.1007/JHEP08(2012)159, arXiv:1103.6083.

[6] ATLAS Collaboration, "Measurement of isolated-photon pair production in pp collisions at $\sqrt{s} = 7$ TeV with the ATLAS detector", *J. High Ener. Phys.* **01** (2013) 086, doi:10.1007/JHEP01(2013)086, arXiv:1211.1913.

[7] CMS Collaboration, "Measurement of differential cross sections for the production of a pair of isolated photons in pp collisions at $\sqrt{s} = 7$ TeV", *Eur.Phys.J.* **C74** (2014), no. 11, 3129, doi:10.1140/epjc/s10052-014-3129-3, arXiv:1405.7225.

[8] CDF Collaboration, "Measurement of the cross section for prompt isolated diphoton production using the full CDF Run II data sample", *Phys.Rev.Lett.* **110** (2013), no. 10, 101801, doi:10.1103/PhysRevLett.110.101801, arXiv:1212.4204.

[9] D0 Collaboration, "Measurement of direct photon pair production cross sections in $p\bar{p}$ collisions at $\sqrt{s} = 1.96$ TeV", *Phys.Lett.* **B690** (2010) 108–117, doi:10.1016/j.physletb.2010.05.017, arXiv:1002.4917.

[10] CMS Collaboration, "Measurement of the isolated prompt photon production cross section in pp collisions at $\sqrt{s} = 7$ TeV", *Phys. Rev. Lett.* **106** (2011) 082001, doi:10.1103/PhysRevLett.106.082001, arXiv:1012.0799.

[11] CMS Collaboration, "Measurement of the production cross section for pairs of isolated photons in pp collisions at $\sqrt{s} = 7$ TeV", *J. High Ener. Phys.* **01** (2012) 133, doi:10.1007/JHEP01(2012)133, arXiv:1110.6461.

[12] CMS Collaboration, "Measurement of the differential cross section for isolated prompt photon production in pp collisions at 7 TeV", *Phys. Rev. D* **84** (2011) 052011, doi:10.1103/PhysRevD.84.052011, arXiv:1108.2044.

[13] CMS Collaboration, "Particle-Flow Event Reconstruction in CMS and Performance for Jets, Taus, and MET", CMS Physics Analysis Summary CMS-PAS-PFT-09-001, 2009.

[14] CMS Collaboration, "Commissioning of the Particle-flow Event Reconstruction with the first LHC collisions recorded in the CMS detector", CMS Physics Analysis Summary CMS-PAS-PFT-10-001, 2010.

[15] CMS Collaboration, "Commissioning of the Particle-Flow reconstruction in Minimum-Bias and Jet Events from pp Collisions at 7 TeV", CMS Physics Analysis Summary CMS-PAS-PFT-10-002, 2010.

[16] CMS Collaboration, "The CMS experiment at the CERN LHC", *J. Inst.* **3** (2008) S08004, doi:10.1088/1748-0221/3/08/S08004.

[17] CMS Collaboration, "Measurement of the inclusive W and Z production cross sections in pp collisions at $\sqrt{s} = 7$ TeV", *J. High Ener. Phys.* **10** (2011) 132, doi:10.1007/JHEP10(2011)132, arXiv:1107.4789.

[18] T. Gleisberg et al., "Event generation with SHERPA 1.1", *J. High Ener. Phys.* **02** (2009) 007, doi:10.1088/1126-6708/2009/02/007, arXiv:0811.4622.

[19] H.-L. Lai et al., "New parton distributions for collider physics", *Phys. Rev. D* **82** (2010) 074024, doi:10.1103/PhysRevD.82.074024, arXiv:1007.2241.

[20] J. Alwall et al., "MadGraph 5: Going Beyond", *J. High Ener. Phys.* **06** (2011) 128, doi:10.1007/JHEP06(2011)128, arXiv:1106.0522.

[21] T. Sjöstrand, S. Mrenna, and P. Z. Skands, "PYTHIA 6.4 Physics and Manual", *J. High Ener. Phys.* **05** (2006) 026, doi:10.1088/1126-6708/2006/05/026, arXiv:hep-ph/0603175.

[22] J. Pumplin et al., "New generation of parton distributions with uncertainties from global QCD analysis", *J. High Ener. Phys.* **07** (2002) 012, doi:10.1088/1126-6708/2002/07/012, arXiv:hep-ph/0201195.

[23] CMS Collaboration, "Measurement of the underlying event activity at the LHC with $\sqrt{s} = 7$ TeV and comparison with $\sqrt{s} = 0.9$ TeV", *J. High Ener. Phys.* **09** (2011) 109, doi:10.1007/JHEP09(2011)109, arXiv:1107.0330.

[24] GEANT4 Collaboration, "GEANT4: A simulation toolkit", *Nucl. Instrum. Meth. A* **506** (2003) 250, doi:10.1016/S0168-9002(03)01368-8.

[25] CMS Collaboration, "Energy calibration and resolution of the CMS electromagnetic calorimeter in pp collisions at $\sqrt{s} = 7$ TeV", *J. Inst.* **8** (2013) P09009, doi:10.1088/1748-0221/8/09/P09009, arXiv:1306.2016.

[26] W. Adam, R. Frühwirth, A. Strandlie, and T. Todorov, "Reconstruction of electrons with the Gaussian-sum filter in the CMS tracker at the LHC", *J. Phys. G* **31** (2005) N9, doi:10.1088/0954-3899/31/9/N01.

[27] M. Cacciari, G. P. Salam, and G. Soyez, "The Anti-k(t) jet clustering algorithm", *JHEP* **0804** (2008) 063, doi:10.1088/1126-6708/2008/04/063, arXiv:0802.1189.

[28] CMS Collaboration, "Determination of Jet Energy Calibration and Transverse Momentum Resolution in CMS", *JINST* **6** (2011) P11002, doi:10.1088/1748-0221/6/11/P11002, arXiv:1107.4277.

[29] CMS Collaboration, "Pileup Jet Identification", CMS Physics Analysis Summary CMS-PAS-JME-13-005, 2013.

[30] M. Cacciari and G. P. Salam, "Pileup subtraction using jet areas", *Phys. Lett. B* **659** (2008) 119, doi:10.1016/j.physletb.2007.09.077, arXiv:0707.1378.

[31] D. L. Rainwater, R. Szalapski, and D. Zeppenfeld, "Probing color singlet exchange in Z + two jet events at the CERN LHC", *Phys.Rev.* **D54** (1996) 6680–6689, doi:10.1103/PhysRevD.54.6680, arXiv:hep-ph/9605444.

[32] G. D'Agostini, "A multidimensional unfolding method based on Bayes theorem", *Nucl. Instrum. Meth. A* **372** (1996) 46, doi:10.1016/0168-9002(95)00274-X.

[33] T. Adye, "Unfolding algorithms and tests using RooUnfold", in *Proceedings of the PHYSTAT 2011 Workshop on Statistical Issues Related to Discovery Claims in Search Experiments and Unfolding*, p. 313. 2011. doi:10.5170/CERN-2011-006.

[34] CMS Collaboration, "Absolute calibration of the luminosity measurement at CMS: Winter 2012 update", CMS Physics Analysis Summary CMS-PAS-SMP-12-008, 2012.

[35] T. Gehrmann, N. Greiner, and G. Heinrich, "Photon isolation effects at NLO in $\gamma\gamma$ + jet final states in hadronic collisions", *JHEP* **1306** (2013) 058, doi:10.1007/JHEP06(2014)076, 10.1007/JHEP06(2013)058, arXiv:1303.0824.

[36] Z. Bern et al., "Next-to-leading order $\gamma\gamma + 2$-jet production at the LHC", *Phys.Rev.* **D90** (2014), no. 5, 054004, doi:10.1103/PhysRevD.90.054004, arXiv:1402.4127.

[37] S. Badger, A. Guffanti, and V. Yundin, "Next-to-leading order QCD corrections to di-photon production in association with up to three jets at the Large Hadron Collider", *JHEP* **1403** (2014) 122, doi:10.1007/JHEP03(2014)122, arXiv:1312.5927.

[38] J. Alwall et al., "The automated computation of tree-level and next-to-leading order differential cross sections, and their matching to parton shower simulations", *JHEP* **1407** (2014) 079, doi:10.1007/JHEP07(2014)079, arXiv:1405.0301.

[39] R. Frederix and S. Frixione, "Merging meets matching in MC@NLO", *JHEP* **1212** (2012) 061, doi:10.1007/JHEP12(2012)061, arXiv:1209.6215.

[40] NNPDF Collaboration, "Parton distributions for the LHC Run II", arXiv:1410.8849.

[41] T. Sjöstrand et al., "An Introduction to PYTHIA 8.2", arXiv:1410.3012.

[42] P. Skands, S. Carrazza, and J. Rojo, "Tuning PYTHIA 8.1: the Monash 2013 Tune", *Eur.Phys.J.* **C74** (2014), no. 8, 3024, doi:10.1140/epjc/s10052-014-3024-y, arXiv:1404.5630.